

# Numerical computation of complex geometrical optics solutions to the conductivity equation

Kari Astala<sup>a</sup>, Jennifer L Mueller<sup>b</sup>, Lassi Päivärinta<sup>a</sup>, Samuli Siltanen<sup>a</sup>

<sup>a</sup>*Department of Mathematics and Statistics, University of Helsinki, Finland*

<sup>b</sup>*Department of Mathematics and School of Biomedical Engineering, Colorado State University, USA*

---

## Abstract

A numerical method is introduced for the evaluation of complex geometrical optics (CGO) solutions to the conductivity equation  $\nabla \cdot \sigma \nabla u(\cdot, k) = 0$  in  $\mathbb{R}^2$  for piecewise smooth conductivities  $\sigma$ . Here  $k$  is a complex parameter. The algorithm is based on the solution by Astala and Päivärinta [Ann. of Math. 163 (2006)] of Calderón's inverse conductivity problem and involves the solution of a Beltrami equation in the plane with an exponential asymptotic condition. The numerical strategy is to solve a related periodic problem using FFT and GMRES and show that the solutions agree on the unit disc. The CGO solver is applied to the problem of computing nonlinear Fourier transforms corresponding to nonsmooth conductivities. These computations give new insight into the D-bar method for the medical imaging technique of electric impedance tomography. Furthermore, the asymptotic behaviour of the CGO solutions as  $k \rightarrow \infty$  is studied numerically. The evidence so gained raises interesting questions about the best possible decay rates for the sub-exponential growth argument in the uniqueness proof for Calderón's problem with  $L^\infty$  conductivities.

*Key words:* inverse problem, Beltrami equation, numerical solver, conductivity equation, inverse conductivity problem, quasiconformal map, complex geometrical optics solution, nonlinear Fourier transform, electrical impedance tomography

*2000 MSC:* 42B10, 65T99

---

## 1. Introduction

We consider the numerical evaluation of *complex geometrical optics* (CGO) solutions to the conductivity equation

$$\nabla \cdot \sigma \nabla u_\sigma = 0 \text{ in } \mathbb{R}^2, \quad (1.1)$$

for piecewise smooth conductivities  $\sigma$ . We assume that  $\sigma$  is measurable and bounded away from 0 and infinity, with  $\sigma(x) \equiv 1$  for  $x$  outside a compact set. The CGO solutions are specified by their asymptotics

$$u_\sigma(z, k) = e^{ikz} \left(1 + \mathcal{O}\left(\frac{1}{z}\right)\right), \text{ as } |z| \rightarrow \infty, \quad (1.2)$$

where  $k \in \mathbb{C}$  is a parameter. The solutions play a key role in solving the fundamental Calderón problem [4, 22, 18, 19, 1, 20, 2], which we next describe in detail.

Suppose that  $\Omega \subset \mathbb{R}^2$  is the unit disc and  $\sigma : \Omega \rightarrow (0, \infty)$  is measurable and satisfies  $0 < c \leq \sigma(z) < \infty$  almost everywhere. Let  $u \in H^1(\Omega)$  be the unique solution to

$$\nabla \cdot \sigma \nabla u = 0 \text{ in } \Omega, \quad (1.3)$$

$$u|_{\partial\Omega} = f \in H^{1/2}(\partial\Omega). \quad (1.4)$$

Static voltage-to-current measurements at the boundary can be modelled by the Dirichlet-to-Neumann map

$$\Lambda_\sigma : H^{1/2}(\partial\Omega) \rightarrow H^{-1/2}(\partial\Omega), \quad f \mapsto \sigma \frac{\partial u}{\partial n} \Big|_{\partial\Omega}.$$

Calderón posed the question in [4] whether  $\sigma$  is uniquely determined by  $\Lambda_\sigma$ , and if so, how to reconstruct  $\sigma$  when  $\Lambda_\sigma$  is given. This problem is also known as Electrical Impedance Tomography (EIT), an imaging technique with applications in medicine, geophysics, and industrial process monitoring [5].

In dimension two Calderón's problem was recently solved using CGO solutions by Astala and Päivärinta [1]. In the case of  $L^\infty$ -conductivities the CGO solutions need to be constructed via the Beltrami equation

$$\bar{\partial}_z f_\mu = \mu \overline{\partial_z f_\mu}, \quad (1.5)$$

where  $\mu$  is a compactly supported  $L^\infty$  function, connected to  $\sigma$  by the identity

$$\mu := \frac{1 - \sigma}{1 + \sigma}. \quad (1.6)$$

Here  $z = z_1 + iz_2 \in \mathbb{C}$  and  $\bar{\partial}_z = (\partial/\partial z_1 + i\partial/\partial z_2)/2$ . Indeed, the respective complex geometric optics solutions are related by the equation

$$2u_\sigma(z, k) = f_\mu(z, k) + f_{-\mu}(z, k) + \overline{f_\mu(z, k)} - \overline{f_{-\mu}(z, k)} \quad (1.7)$$

The simple reason behind these identities is that the real part  $u$  of  $f_\mu(z, k)$  solves the equation (1.1) while the imaginary part solves the same equation with  $\sigma$  replaced by  $1/\sigma$ .

An asymptotic condition similar to (1.2) is required:

$$f_\mu(z, k) = e^{ikz}(1 + \omega(z, k)) \quad \text{with} \quad \omega(z, k) = \mathcal{O}\left(\frac{1}{z}\right) \text{ as } |z| \rightarrow \infty. \quad (1.8)$$

In particular, constructing solutions to (1.1) is now reduced to considering the Beltrami equation (1.5).

In this paper we introduce a numerical algorithm for the computation of the CGO solutions  $f_\mu$  of the form (1.8), satisfying the Beltrami equation (1.5) for a given  $\mu = (1-\sigma)/(1+\sigma)$ . Simultaneously we obtain the CGO solutions  $u_\sigma$  for the conductivity equation (1.1). We assume that  $\sigma$  is piecewise continuous in the following sense.

**Definition 1.** *We say that  $\sigma$  is piecewise continuous if  $\sigma \in C^0(\Omega \setminus \Gamma)$ , where  $\Gamma$  is the union of a finite number of piecewise  $C^1$  curves  $\Gamma_i : [0, 1] \rightarrow \Omega$  for which  $\Gamma_i \cap \Gamma_j$  is a discrete set whenever  $i \neq j$ .*

This is a reasonable assumption for medically relevant conductivities. The algorithm is based on periodization, truncation of a Neumann series, discretization, and the use of fast Fourier transform and the iterative GMRES solver. The basic ideas for the numerical part of this work come from Vainikko's solution method [24] for the Lippmann-Schwinger equation, and from the generalization of that method for the  $\bar{\partial}$  equation by Knudsen, Mueller and Siltanen [15]. We remark that the present generalization of [24] is more complicated than the one reported in [15].

Numerical computation of solutions to the Beltrami equation have been described in [9, 6]. Those two approaches do not apply to the exponential asymptotic condition (1.8) of interest here.

We verify our new algorithm by comparison to Faddeev's CGO solutions for the Schrödinger equation [8]. Those solutions are used in Nachman's uniqueness proof [18] for Calderón's problem assuming twice differentiable conductivities. The numerical computation of these solutions, henceforth called the *benchmark method*, is already well understood [20, 16]. Equation (1.7) leads to a simple formula connecting the two CGO solutions when the conductivity is smooth, and we can check that the two algorithms agree. In fact, for  $k$  close to zero the new algorithm is found to give more accurate results than the benchmark method.

Applications of our new algorithm include

- (i) Checking intermediate results when developing EIT algorithms based on [1],
- (ii) Evaluating Faddeev's CGO solutions accurately for  $k$  near zero,
- (iii) Computing nonlinear Fourier transforms numerically,

(iv) Studying quasiconformal mappings.

Goal (i) is a large project of its own and will not be discussed further here. Concerning (iii), we compute for the first time the scattering transform (also called the nonlinear Fourier transform)  $\mathbf{t} : \mathbb{C} \rightarrow \mathbb{C}$  corresponding to a *discontinuous* conductivity. For this, we provide new insight by numerical experiments. Our results suggest that for nonsmooth conductivities there may not exist large  $|k|$  estimates of the form  $|\mathbf{t}(k)| \leq C|k|^\lambda$  with  $\lambda \leq 0$ . Note that in the smooth case it is known [20, Theorem 3.2] that  $|\mathbf{t}(k)| \leq |k|^{-m}$  for large  $|k|$  if  $\sigma \in C^{2+m}(\Omega)$  and  $m \geq 1$ . Approximate scattering transforms for discontinuous conductivities were studied in [14].

As a contribution to (iv) we study numerically the behaviour of  $f_\mu(\cdot, k)$  when  $|k|$  grows. It was proven in [1] that  $f_\mu(z, k) = \exp(ik\phi_\mu(z, k))$ , where  $\phi_\mu$  is a quasiconformal homeomorphism satisfying  $\phi_\mu(z, k) = z + \mathcal{O}(1/z)$  when  $z \rightarrow \infty$ . The technically most demanding result in [1], crucially important for the uniqueness proof, is establishing the following subexponential growth result:  $\lim_{k \rightarrow \infty} \phi_\mu(z, k) = z$  uniformly in  $z \in \mathbb{C}$ . Our computation yields numerical evidence for the existence of an estimate of the form  $\sup_{z \in \Omega} |\phi_\mu(z, k) - z| \leq C|k|^\lambda$  with  $\lambda < 0$  in the case of simple piecewise smooth discontinuous conductivity. This raises the very interesting question what are the best possible theoretical decay rates in this context.

This paper is organized as follows. In Section 2 we derive a periodic construction of the CGO solutions  $f_\mu$ . The Neumann series so achieved is truncated in Section 3 to give a numerically viable approximation to the CGO solutions, and in Section 4 we describe an algorithm for the evaluation of those approximations. In Section 5 we discuss CGO solutions for the Schrödinger equation, derive a connection between the two solution types, and verify the new CGO solver by comparison to the benchmark method. In Section 6 we apply our method to the evaluation of nonlinear Fourier transforms corresponding to discontinuous conductivities. Section 7 is devoted to the numerical study of  $\phi_\mu(\cdot, k)$  as  $k$  grows. Finally, in Section 8 we discuss hardware issues and give directions for further study of efficiency and accuracy of our new method.

## 2. Construction of CGO solutions via periodization

The CGO solutions are constructed in [1] as follows. Define the solid Cauchy transform by

$$Pf(z) = -\frac{1}{\pi} \int_{\mathbb{C}} \frac{f(\lambda)}{\lambda - z} dm(\lambda), \quad (2.1)$$

and Beurling transform by  $Sf = \partial Pf$ . Note that  $P$  is the inverse operator of  $\bar{\partial}$  and that  $S$  transforms  $\bar{\partial}$  derivatives into  $\partial$  derivatives:  $S(\bar{\partial}f) = \partial f$ .

Let  $\Omega$  denote the unit disc. For given piecewise continuous conductivity  $\sigma : \Omega \rightarrow \mathbb{R}$  and any complex number  $k \in \mathbb{C}$ , set  $\mu = (1 - \sigma)/(1 + \sigma)$  and define

$$\alpha(z, k) = -i\bar{k}e_{-k}(z)\mu(z), \quad (2.2)$$

$$\nu(z, k) = e_{-k}(z)\mu(z), \quad (2.3)$$

where  $e_{-k}(z) := \exp(-i(kz + \bar{k}\bar{z}))$ . Then  $\alpha(\cdot, k), \nu(\cdot, k) \in L^\infty(\Omega)$  and  $|\nu(z, k)| = |\mu(z, k)| \leq \kappa < 1$  for almost every  $z$ . The following theorem was proven in [1].

**Theorem 1.** (*Astala and Päivärinta*) *Let  $k \in \mathbb{C}$ . Assume that  $\alpha(\cdot, k) \in L^\infty(\Omega)$  and  $\nu(\cdot, k) \in L^\infty(\Omega)$  and  $|\nu(z, k)| \leq \kappa < 1$  for almost every  $z$ . Take  $2 < p < 1 + 1/\kappa$  and define the operator  $K : L^p(\mathbb{C}) \rightarrow L^p(\mathbb{C})$  by*

$$Kg = P(I - \nu\bar{S})^{-1}(\alpha\bar{g}). \quad (2.4)$$

*Then  $K : L^p(\mathbb{C}) \rightarrow W^{1,p}(\mathbb{C})$  and  $I - K$  is invertible in  $L^p(\mathbb{C})$ . Further, equation*

$$(I - K)\omega = K(\chi_\Omega) \quad (2.5)$$

*has a unique solution with asymptotics  $\omega(z, k) = \mathcal{O}(1/z)$ .*

Let us recall the definition of the Sobolev space  $W^{1,p}(\mathbb{C})$ :

$$W^{1,p}(\mathbb{C}) = \{f \in L^p(\mathbb{C}) \mid \frac{\partial f}{\partial z_j} \in L^p(\mathbb{C}) \text{ for } j = 1, 2\}.$$

We note that the Sobolev imbedding theorem implies that  $W^{1,p}(\mathbb{C})$  functions are continuous when  $p > 2$ .

The complex geometrical optics solutions  $f_\mu$  are given by substituting the unique solution of equation (2.5) to formula (1.8). Next we derive a periodic equation equivalent to (2.5) and more suitable for numerical solution.

According to [21] the Beurling transform  $S$  has the properties

$$S : L^r(\mathbb{C}) \longrightarrow L^r(\mathbb{C}), \quad 1 < r < \infty, \quad \text{and} \quad \|S\|_{L^2 \rightarrow L^2} = 1. \quad (2.6)$$

Thus  $\|\nu\bar{S}\|_{L(L^2(Q))} < 1$ , and consequently  $(I - \nu\bar{S})^{-1}$  can be expressed as a Neumann series. Denoting complex conjugation as an operator  $\rho(f) = \bar{f}$ , we see that  $\omega$  satisfies

$$\bar{\partial}\omega = (I - \nu\bar{S})^{-1}(\alpha\bar{\omega} + \alpha) = \sum_{\ell=0}^{\infty} (\nu\rho\partial P)^\ell(\alpha\bar{\omega} + \alpha). \quad (2.7)$$

By the uniqueness result for equation (2.5), equation (2.7) has a unique solution with asymptotics  $\omega(z, k) = \mathcal{O}(1/z)$ .

Take  $\epsilon > 0$  and set  $s = 2 + 3\epsilon$ . Define  $Q := [-s, s]^2$  and introduce a periodic version of equation (2.5) as follows. Choose an infinitely smooth cutoff function  $\eta \in C_0^\infty(\mathbb{R}^2)$  satisfying

$$\eta(z) = \begin{cases} 1 & \text{for } |z| < 2 + \epsilon, \\ \text{smooth} & \text{for } 2 + \epsilon \leq |z| < 2 + 2\epsilon, \\ 0 & \text{for } |z| \geq 2 + 2\epsilon, \end{cases} \quad (2.8)$$

and  $0 \leq \eta(z) \leq 1$  for all  $z \in \mathbb{C}$ .

Define a  $2s$ -periodic approximate Green's function  $\tilde{g}$  by setting it to  $\eta(z)/(\pi z)$  inside  $Q$  and extending periodically:

$$\tilde{g}(z + j2s + i\ell 2s) = \frac{\eta(z)}{\pi z} \quad \text{for } z \in Q \setminus 0, \quad j, \ell \in \mathbb{Z}. \quad (2.9)$$

Define a periodic approximate Cauchy transform by

$$\tilde{P}f(z) = (\tilde{g} \tilde{*} f)(z) = \int_Q \tilde{g}(z - w)f(w)dw, \quad (2.10)$$

where  $\tilde{*}$  denotes convolution on the torus; then  $\tilde{P}$  is a compact operator on  $L^2(Q)$ . We introduce the periodic counterpart of  $K$  as follows:

$$\tilde{K}\varphi = \tilde{P}(I - \nu\rho\partial\tilde{P})^{-1}(\alpha\bar{\varphi}) = \tilde{P}\sum_{\ell=0}^{\infty}(\nu\rho\partial\tilde{P})^\ell(\alpha\bar{\varphi}), \quad (2.11)$$

where the compactly supported functions  $\nu$  and  $\alpha$  are periodically extended in the obvious way. Then the operator  $\tilde{K} : L^2(Q) \rightarrow L^2(Q)$  is compact.

**Theorem 2.** *Let  $k \in C$ . There exists a unique  $2s$ -periodic solution to equation*

$$(I - \tilde{K})\tilde{\omega} = \tilde{K}(\chi_\Omega), \quad (2.12)$$

where  $\chi_\Omega$  is periodically extended. Furthermore, the solutions of (2.5) and (2.12) agree on the unit disc:  $\omega(z, k) = \tilde{\omega}(z, k)$  for  $z \in \Omega$ .

**Proof.** Assume  $\tilde{\omega}_1$  and  $\tilde{\omega}_2$  are solutions of (2.12). We will show that  $\tilde{\omega}_1 = \tilde{\omega}_2$ .

Let  $\varphi$  be a function with  $\text{supp}(\varphi) \subset \Omega$ , and denote by  $\tilde{\varphi}$  the periodic extension of  $\varphi$ . Since the functions  $(\pi\zeta)^{-1}$  and  $\tilde{g}(\zeta)$  coincide for  $|\zeta| = |z - w| < 2 + \epsilon$ , the following identity holds for  $|z| < 1 + \epsilon$ :

$$(P\varphi)(z) = \frac{1}{\pi} \int_\Omega \frac{\varphi(w)}{z - w} dw = \int_Q \tilde{g}(z - w)\tilde{\varphi}(w)dw = (\tilde{P}\tilde{\varphi})(z). \quad (2.13)$$

Define two non-periodic functions  $\omega_1, \omega_2 : \mathbb{R}^2 \rightarrow \mathbb{C}$  by the formulae

$$\omega_j(z) = \tilde{\omega}_j(z) \quad \text{for } |z| < 1 + \epsilon, \quad (2.14)$$

$$\omega_j(z) = P(I - \nu\rho\partial P)^{-1}(\alpha\overline{\tilde{\omega}_j|_Q} + \alpha), \quad \text{for } |z| > 1. \quad (2.15)$$

The formulae (2.14) and (2.15) agree in the annulus  $1 < |z| < 1 + \epsilon$ . To see this note that since  $\tilde{\omega}_j$  are solutions of (2.12) for  $j = 1, 2$ , we have

$$\tilde{\omega}_j = \tilde{P}(I + \nu\rho\partial\tilde{P} + (\nu\rho\partial\tilde{P})^2 + \dots)(\alpha\overline{\tilde{\omega}_j} + \alpha), \quad j = 1, 2. \quad (2.16)$$

Because both  $\alpha\overline{\tilde{\omega}_j} + \alpha$  and  $(I + \nu\rho\partial\tilde{P} + (\nu\rho\partial\tilde{P})^2 + \dots)(\alpha\overline{\tilde{\omega}_j} + \alpha)$  are supported in the unit disc, repeated applications of (2.13) to the identity (2.16) yield the claim.

Applying the  $\bar{\partial}$  derivative to both sides of (2.16) and using (2.13) shows that  $\omega_1$  and  $\omega_2$  satisfy equation (2.7) in the disc  $|z| < 1 + \epsilon$ . Further, applying the  $\bar{\partial}$  derivative to both sides of (2.15) and substituting (2.14) shows that  $\omega_1$  and  $\omega_2$  satisfy equation (2.7) for  $|z| > 1$ . Thus  $\omega_1$  and  $\omega_2$  satisfy (2.7) everywhere.

Since  $(I - \nu\rho\partial P)^{-1}(\alpha\overline{\tilde{\omega}_j|_Q} + \alpha)$  is supported in the unit disc, formula (2.15) together with (2.1) implies that  $\omega_j(z) = \mathcal{O}(1/z)$  for large  $|z|$ . By uniqueness of solutions to equation (2.7) we conclude that  $\omega_1 = \omega_2$ .

By formula (2.14) we thus know that  $\tilde{\omega}_1(z, k) = \tilde{\omega}_2(z, k)$  for  $|z| \leq 1$ , and another application of (2.16) and the argument above shows that actually  $\tilde{\omega}_1(z, k) = \tilde{\omega}_2(z, k)$  for all  $z \in Q$ . Finally, since  $\tilde{K}$  is a compact operator on  $L^2(Q)$ , the solvability of (2.12) follows by the Fredholm alternative.

The solutions of (2.5) and (2.12) are now seen to agree on  $\Omega$  simply by (2.14).

Q.E.D.

**Corollary 1.** *Given the solution  $\tilde{\omega}$  of the periodic equation (2.12), the solution  $\omega : \mathbb{R}^2 \rightarrow \mathbb{C}$  of equation (2.5) can be written as*

$$\omega = P(I - \nu\bar{S})^{-1}(\alpha\overline{\tilde{\omega}|_\Omega} + \alpha).$$

### 3. Approximate CGO solutions

The inverse operator appearing in the definition (2.11) of operator  $\tilde{K}$  is difficult to deal with numerically. Thus we introduce a computationally feasible equation whose solutions approximate the periodic CGO solutions.

Define the truncated periodic operator  $\tilde{K}_L$  by the formula

$$\tilde{K}_L(\varphi) := \tilde{P} \sum_{\ell=0}^L (\nu\rho\partial\tilde{P})^\ell (\alpha\overline{\varphi}). \quad (3.1)$$

Then the convergence of the Neumann series in (2.11) implies the following:

$$\lim_{L \rightarrow \infty} \|\tilde{K}(\chi_\Omega) - \tilde{K}_L(\chi_\Omega)\|_{L^2(Q)} = 0, \quad (3.2)$$

$$\lim_{L \rightarrow \infty} \|\tilde{K} - \tilde{K}_L\|_{L(L^2(Q))} = 0. \quad (3.3)$$

**Theorem 3.** *Let  $\varepsilon > 0$  and take any  $k \in \mathbb{C}$ . Then there is such  $L_0 > 0$  that for all  $L > L_0$  there exists a unique  $2s$ -periodic solution to the equation*

$$(I - \tilde{K}_L) \tilde{\omega}_L = \tilde{K}_L(\chi_\Omega). \quad (3.4)$$

*Furthermore, there is such  $L_\varepsilon \geq L_0$  that for all  $L > L_\varepsilon$ , the unique solutions of equations (3.4) and (2.12) satisfy*

$$\|\tilde{\omega}(\cdot, k) - \tilde{\omega}_L(\cdot, k)\|_{L^2(Q)} \leq \varepsilon. \quad (3.5)$$

**Proof.** Combine (3.2) and (3.3) with

$$\begin{aligned} \tilde{\omega} - \tilde{\omega}_L &= (I - \tilde{K})^{-1} \tilde{K}(\chi_\Omega) - (I - \tilde{K}_L)^{-1} \tilde{K}_L(\chi_\Omega) \\ &= (I - \tilde{K})^{-1} \{ \tilde{K}(\chi_\Omega) - \tilde{K}_L(\chi_\Omega) \} \\ &\quad - \{ (I - \tilde{K})_L^{-1} - (I - \tilde{K})^{-1} \} \tilde{K}_L(\chi_\Omega), \end{aligned}$$

and use standard functional analytic arguments. Q.E.D.

**Corollary 2.** *Let  $k \in \mathbb{C}$ . For all large enough  $L > 0$  define*

$$\omega_L(z, k) = P(I - \nu \bar{S})^{-1}(\alpha \overline{\tilde{\omega}_L|_\Omega} + \alpha),$$

*where  $\tilde{\omega}_L$  is the solution of equation (3.4). Then the solution  $\omega : \mathbb{R}^2 \rightarrow \mathbb{C}$  of equation (2.5) satisfies*

$$\lim_{L \rightarrow \infty} \|\omega_L(\cdot, k) - \omega(\cdot, k)\|_{L^2(\mathbb{C})} = 0.$$

**Proof.** Combine Corollary 1 with Theorem 3 and the continuity of the operators  $P$  and  $(I - \nu \bar{S})^{-1}$ . Q.E.D.

#### 4. Computational algorithm for approximate CGO solutions

In a manner similar to [15], we modify the numerical Lippmann-Schwinger solver of Vainikko [24] for solving  $\tilde{\omega}_L$  from equation (3.4). Then Corollary 2 implies that we can evaluate  $\omega$  with arbitrary accuracy.

##### 4.1. Discretization of periodic functions

As in Section 2, take a square  $Q := [-s, s]^2$  with some  $s > 2$  as the basic tile of periodic tessellation of the plane. Choose a positive integer  $m$ , denote  $M = 2^m$ , and set  $h = 2s/M$ . Define a grid  $\mathcal{G}_m \subset Q$  by

$$\begin{aligned} \mathcal{G}_m &= \{jh \mid j \in \mathbb{Z}_m^2\}, \\ \mathbb{Z}_m^2 &= \{j = (j_1, j_2) \in \mathbb{Z}^2 \mid -2^{m-1} \leq j_\ell < 2^{m-1}, \ell = 1, 2\}. \end{aligned} \quad (4.1)$$

Note that the number of points in  $\mathcal{G}_m$  is  $M^2$ . Define the grid approximation  $\varphi_h : \mathbb{Z}_m^2 \rightarrow \mathbb{C}$  of a function  $\varphi : Q \rightarrow \mathbb{C}$  by

$$\varphi_h(j) = \varphi(jh). \quad (4.2)$$

#### 4.2. Implementation of the Cauchy transform

Consider the periodic approximate Cauchy transform  $\tilde{P}$  defined in (2.10). Choose a cutoff function  $\eta$  as in (2.8), recall the periodic approximate Green's function  $\tilde{g}$  defined in (2.9), and set

$$\tilde{g}_h(j) = \begin{cases} \tilde{g}(jh), & \text{for } j \in \mathbb{Z}_m^2 \setminus 0, \\ 0, & \text{for } j = 0; \end{cases} \quad (4.3)$$

note that here the point  $jh \in \mathbb{R}^2$  is interpreted as the complex number  $hj_1 + ihj_2$ . Now  $\tilde{g}_h$  is simply a  $M \times M$  matrix with complex entries. Given a periodic function  $\varphi$ , the transform  $\tilde{P}\varphi$  is approximately given by

$$(\tilde{P}\varphi)_h = h^2 \mathcal{F}^{-1}(\mathcal{F}(\tilde{g}_h) \cdot \mathcal{F}(\varphi_h)), \quad (4.4)$$

where  $\mathcal{F}$  stands for discrete Fourier transform (DFT) and  $\cdot$  denotes element-wise matrix multiplication. This approach is based on the fact that convolution  $\tilde{*}$  on the torus becomes multiplication under DFT. Note that the grid  $\mathcal{G}_m$  is defined so that fast Fourier transform is readily applicable to (4.4).

#### 4.3. Implementation of the Beurling transform

We could follow the theoretical treatment of Section 2 closely and write  $(\tilde{S}\varphi)_h = D_h(\tilde{P}\varphi)_h$  with  $D_h$  a finite difference approximation to  $\partial$ . Another approach would be to approximate the Fourier multiplier  $m(\xi) = -\xi/\bar{\xi}$  on the discrete Fourier transform side by some  $\tilde{m}(\xi)$  and set  $(\tilde{S}\varphi)_h = h^2 \mathcal{F}^{-1}(\tilde{m}_h \cdot \mathcal{F}(\varphi_h))$ . However, after numerical testing we found that the following implementation based on convolution works best for us in terms of accuracy, speed, and ease of programming.

The Beurling transform for functions defined on  $\mathbb{C}$  can be written as a principal value integral

$$Sg(z) = -\frac{1}{\pi} \int_{\mathbb{C}} \frac{g(w)}{(w-z)^2} dw.$$

We approximate  $S$  in our periodic context by writing

$$\tilde{\beta}(z + j2s + i\ell 2s) = \frac{\eta(z)}{\pi z^2} \quad \text{for } z \in Q \setminus 0, \quad j, \ell \in \mathbb{Z},$$

where  $\eta(z)$  is defined by (2.8), and defining

$$\tilde{S}g(z) := (\tilde{\beta} \tilde{*} g)(z) = \int_Q \tilde{\beta}(z-w)g(w)dw.$$

The discrete transform is given by

$$(\tilde{S}\varphi)_h = h^2 \mathcal{F}^{-1}(\mathcal{F}(\tilde{\beta}_h) \cdot \mathcal{F}(\varphi_h)), \quad (4.5)$$

where  $\tilde{\beta}_h$  is the complex-valued  $M \times M$  matrix

$$\tilde{\beta}_h(j) = \begin{cases} \tilde{\beta}(jh), & \text{for } j \in \mathbb{Z}_m^2 \setminus 0, \\ 0, & \text{for } j = 0. \end{cases} \quad (4.6)$$

#### 4.4. Implementation of the operator $\tilde{K}_L$

How should one choose the truncation index  $L$  in the expression

$$\tilde{K}_L(\varphi) := \tilde{P} \sum_{\ell=0}^L (\nu \rho \tilde{S})^\ell (\alpha \bar{\varphi})?$$

It is difficult in practice to find a large enough  $L$  in the sense of Theorem 3, so instead we use truncation based on a tolerance criterion. Choose some  $0 < \tau < 1$  and set

$$L := \min\{\ell > 0 : \|(\nu \rho \tilde{S})^\ell (\alpha \bar{\varphi})\|_{L^2(Q)} < \tau \|\alpha \bar{\varphi}\|_{L^2(Q)}\}. \quad (4.7)$$

After fixing  $L$  using (4.7), the computation of  $(\tilde{K}_L(\varphi_h))_h$  for a given grid approximation  $\varphi_h$  is a combination of element-wise matrix multiplications, complex conjugations, and applications of the approximate operators  $\tilde{P}$  and  $\tilde{S}$  as explained in Sections 4.2 and 4.3.

#### 4.5. Numerical solution of equation (3.4)

Computation of  $\tilde{\omega}_L$  starts with the evaluation of the right hand side of (3.4) with  $L$  given by (4.7):

$$\tilde{K}_L(\chi_\Omega) = \tilde{P} \sum_{\ell=0}^L \left( \nu \bar{\tilde{S}} \right)^\ell \alpha. \quad (4.8)$$

This is straightforward as explained in Section 4.4.

The solution of equation (3.4) is implemented by a matrix-free iterative method, such as generalized minimal residual method (GMRES). In iterative methods it is enough to provide a numerical algorithm for the mapping  $\varphi_h \mapsto (\varphi_h - (\tilde{K}_L(\varphi_h))_h)$ , which we essentially described above. Note that since the operator  $\tilde{K}_L$  is not complex linear but only real-linear, we need to treat the real and imaginary parts separately so that GMRES is applied to a real-linear problem of dimension  $2^{2m+1}$ .

## 5. Numerical verification of the solver

We have previously implemented a numerical algorithm [16], here called the benchmark method, for the evaluation of complex geometrical optics solutions for the conductivity equation used by Nachman in [18]. The CGO solutions considered in this work are connected by rather simple relations to Nachman's solutions in the case of smooth conductivities, and thus we can verify our new algorithm by comparing it to the benchmark method for a smooth example conductivity.

Since the new method makes no significant distinction between smooth and piecewise smooth conductivities, we will assume that it works for discontinuous  $\sigma$  if it works for smooth  $\sigma$ .

### 5.1. Complex geometrical optics solutions via the Schrödinger equation

Assume that  $\sigma$  is twice continuously differentiable and that  $\sigma \equiv 1$  near the boundary  $\partial\Omega$ . Nachman [18] defines  $q_1 = \sigma^{-1/2}\Delta\sigma^{1/2}$  with zero extension outside  $\Omega$  and considers the CGO solutions

$$(-\Delta + q_1)\psi_1(\cdot, k) = 0 \quad \text{in } \mathbb{R}^2 \quad (5.1)$$

first introduced by Faddeev [8]. By [18, Thm.1.1] for any  $k \in \mathbb{C} \setminus 0$  there is a unique solution  $\psi_1$  of (5.1) satisfying

$$e^{-ikz}\psi_1(z, k) - 1 \in W^{1,p}(\mathbb{R}^2) \quad (5.2)$$

for any  $2 < p < \infty$ .

The solutions  $\psi_1$  of (5.1) satisfying (5.2) are constructed via the definition

$$m_1(z, k) := e^{-ikz}\psi_1(z, k), \quad z \in \mathbb{R}^2, k \in \mathbb{C} \setminus 0. \quad (5.3)$$

The function  $m_1$  is the unique solution of the Lippmann-Schwinger type equation

$$m_1 = 1 - g_k * (q_1 m_1) \quad (5.4)$$

satisfying  $m_1 - 1 \in W^{1,p}(\mathbb{R}^2)$ , where  $*$  denotes convolution of functions defined on  $\mathbb{R}^2$ . The Faddeev fundamental solution  $g_k$  is given by

$$g_k(z) := \frac{1}{(2\pi)^2} \int_{\mathbb{R}^2} \frac{e^{iz \cdot \xi}}{|\xi|^2 + 2k(\xi_1 + i\xi_2)} d\xi, \quad (5.5)$$

and satisfies  $(-\Delta - 4ik\bar{\partial})g_k = \delta_0$ . Here  $\delta_0$  denotes Dirac's delta distribution. We remark that numerical evaluation of  $g_k(z)$  was introduced in [20] and optimized in [10].

We repeat the above construction for the conductivity  $1/\sigma$ . Define  $q_2 = \sigma^{1/2}\Delta\sigma^{-1/2}$  and consider the unique solution of the Schrödinger equation

$$(-\Delta + q_2)\psi_2(\cdot, k) = 0 \quad (5.6)$$

with the asymptotic condition  $e^{-ikz}\psi_2(z, k) - 1 =: m_2(z, k) - 1 \in W^{1,p}(\mathbb{R}^2)$ . Then

$$u_1(z, k) := \sigma^{-1/2}(z)e^{ikz}m_1(z, k), \quad (5.7)$$

$$u_2(z, k) := \sigma^{1/2}(z)e^{ikz}m_2(z, k), \quad (5.8)$$

are the unique solutions of the following two conductivity equations:

$$\nabla \cdot \sigma \nabla u_1 = 0, \quad u_1 \sim e^{ikz}, \quad (5.9)$$

$$\nabla \cdot \sigma^{-1} \nabla u_2 = 0, \quad u_2 \sim e^{ikz}. \quad (5.10)$$

Note that in [1] the asymptotic behaviour of  $u_2$  is  $ie^{ikz}$  but in this paper it is  $e^{ikz}$ .

### 5.2. Connection between the CGO solutions $\psi_1, \psi_2$ and $f_\mu$

From (1.6) we see that  $-\mu$  relates to  $1/\sigma$  the same way that  $\mu$  relates to  $\sigma$ . Set

$$h_+ = \frac{1}{2}(f_\mu + f_{-\mu}), \quad h_- = \frac{1}{2}(\overline{f_\mu} - \overline{f_{-\mu}});$$

note that the above definition of  $h_-$  differs from [1] by an  $i$ . Now  $h_+ - ih_-$  and  $i(h_+ + ih_-)$  are solutions of (5.9) and (5.10), respectively, and by uniqueness  $u_1 = h_+ - ih_-$  and  $u_2 = i(h_+ + ih_-)$ . So we can write

$$f_\mu = (u_1 + \overline{u_1})/2 + (u_2 - \overline{u_2})/2,$$

and substituting (1.8), (5.7) and (5.8) gives the desired connection:

$$\omega(z, k) = -1 + e^{-ikz} [\operatorname{Re}(\sigma^{-1/2} e^{ikz} m_1(z, k)) + i \operatorname{Im}(\sigma^{1/2} e^{ikz} m_2(z, k))]. \quad (5.11)$$

### 5.3. Computational results

We define a smooth example conductivity  $\sigma$  resembling the transversal cross-section of human chest. The region of higher conductivity than background simulates a heart filled with blood, while the two regions with lower conductivity than background model lungs filled with air. See Figure 1 for plots of conductivities  $\sigma$  and  $1/\sigma$  and their respective potentials  $q_1$  and  $q_2$ .

We choose a set  $\mathcal{K} := \{k^{(1)}, k^{(2)}, \dots, k^{(48)}\} \subset \mathbb{C}$  of complex numbers with six different moduli between 1 and 16, and eight fixed arguments. See Figure 2.

We take  $Q := [-s, s]^2$  with  $s = 2.3$  and compute  $m_1(\cdot, k^{(\ell)})$  and  $m_2(\cdot, k^{(\ell)})$  for every  $\ell = 1, \dots, 48$  with the benchmark method. We perform the computation on two grids of the form (4.1): on  $\mathcal{G}_9$  having  $512 \times 512$  points and on  $\mathcal{G}_{10}$  comprising  $1024 \times 1024$  points. By construction we have  $\mathcal{G}_9 \subset \mathcal{G}_{10}$ , so we can directly compare the values of solutions on  $\mathcal{G}_9$ . The relative sup norm error between the two results is 7% for points in  $\mathcal{K}$  with  $|k| = 1$  and less than 2% for  $|k| \geq 4$ .

Next we evaluate  $\tilde{\omega}_L(\cdot, k^{(\ell)})$  for  $\ell = 1, \dots, 48$  on grids  $\mathcal{G}_8$  and  $\mathcal{G}_9$ . For this, we introduce a radially piecewise linear cutoff function

$$\eta(z) = \begin{cases} 1 & \text{for } |z| < 2.07, \\ \text{linear} & \text{for } 2.07 \geq |z| < 2.3, \\ 0 & \text{for } |z| \geq 2.3. \end{cases}$$

According to the theory, of course, the function  $\eta$  should be infinitely smooth as in (2.8). However, we believe that in practical computation the piecewise linear cutoff function performs well enough.

The computation of the function  $\tilde{\omega}_L(\cdot, k)$  defined in (3.4) for a given  $k \in \mathbb{C}$  and  $z$ -grid  $\mathcal{G}$  proceeds as follows.

**Step 1.** For every  $z \in \mathcal{G}$ , evaluate the functions  $\alpha(z)$  and  $\nu(z)$  defined in (2.2) and (2.3), respectively.

Figure 1: Smooth example conductivity, its inverse, and the corresponding Schrödinger potentials. In each plot  $z_1$  and  $z_2$  both range in the interval  $[-1, 1]$ .

Figure 2: Black dots denote the complex points  $k^{(1)}, k^{(2)}, \dots, k^{(48)}$  used for testing the accuracy of the computation of CGO solutions. The radii of the points in the collection are indicated on the real axis. The origin of the  $k$  plane is in the center of the picture.

- Step 2.** For every  $z \in \mathcal{G}$ , evaluate the function  $\chi_\Omega(z)$ . Then compute  $\tilde{K}_L(\chi_\Omega)$  using formula (3.1) involving  $\alpha(z)$  and  $\nu(z)$  available from the previous step. The Cauchy and Beurling transforms appearing in (3.1) are implemented as explained in Sections 4.3 and 4.3, respectively. We use  $\tau = 10^{-5}$  as the tolerance in the criterion (4.7) for  $L$ .
- Step 3.** Numerical solution of equation (3.4) for  $\tilde{\omega}_L(\cdot, k)$  is based on the iterative GMRES solver, as explained in Section 4.5. The right hand side of (3.4) is now available from the previous step.

See Figures 3 and 4 for plots of some solutions  $\tilde{\omega}_L$ . We remark that we give  $\tilde{K}_L(\chi_\Omega)$  as initial guess for the GMRES solver when working on the  $256 \times 256$  grid, and the result of that computation as initial guess for the computation using  $512 \times 512$  grid points, and use the GMRES solver without a preconditioner.

The relative error between the left and right hand sides of equation (5.11) is defined by the average value of the relative errors at a given radius  $R$

$$E(R) := \frac{1}{8} \sum_{k \in \mathcal{K}, |k|=R} \frac{\max |\text{lhs}(5.11) - \text{rhs}(5.11)|}{\max |\text{rhs}(5.11)|}, \quad (5.12)$$

where in the right hand side we use the solutions  $m_1(\cdot, k^{(\ell)})$  and  $m_2(\cdot, k^{(\ell)})$  computed on the grid  $\mathcal{G}_{10}$  projected to the grids  $\mathcal{G}_8$  and  $\mathcal{G}_9$  appropriately. Computational errors are provided in Table 1.

#### 5.4. Discussion of errors

The inaccuracy in the computations of  $m_1(\cdot, k)$  and  $m_2(\cdot, k)$  for  $k$  near zero stems from the fact that Faddeev's fundamental solution  $g_k$  in equation (5.4) has a  $\log |k|$  singularity at  $k = 0$ . In contrast, solving equation (2.5) for  $\omega(z, k)$  does not involve the computation of any function with a singularity at  $k = 0$ . It is for this reason that in Table 1 the left and right hand sides

	$R = 1$	$R = 4$	$R = 7$	$R = 10$	$R = 13$	$R = 16$
Grid size						
$256 \times 256$	3.0%	0.7%	0.4%	0.5%	1.0%	1.8%
$512 \times 512$	3.0%	0.7%	0.3%	0.2%	0.3%	0.5%

Table 1: Relative sup norm errors  $E(\varrho)$  of numerically computed left and right hand sides of equation (5.11). Exact definition of the relative error is given in formula (5.12). The non-convergence in cases  $R = 1$  and  $R = 4$  results from difficulties in evaluating the right hand side using the benchmark method.

Figure 3: Real and imaginary parts of  $\tilde{\omega}_L(z, 1)$ . Here  $z$  ranges in the unit disc. The scale of the vertical axis is the same in both plots.

Figure 4: Real and imaginary parts of  $\tilde{\omega}_L(z, -4.9497 - 4.9497i)$ . Here  $z$  ranges in the unit disc. The scale of the vertical axis is the same in both plots.

of (5.11) agree quite well numerically for sufficiently large  $|k|$ , and the error becomes smaller as the grid is refined, but for smaller  $|k|$  values (the cases  $R = 1$  and  $R = 4$ ), similar convergence results are not obtained. In summary, this lack of convergence reflects the inaccuracy of the benchmark method for small  $|k|$  rather than that of the new method.

We may thus conclude that our solver produces accurate CGO solutions for the Beltrami equation for  $|k| \leq 16$ , at least in the case of a smooth medium-contrast conductivity.

## 6. Computing nonlinear Fourier transforms

Let us recall the scattering transform  $\mathbf{t} : \mathbb{C} \rightarrow \mathbb{C}$  considered by Nachman in [18] (and previously used in higher dimensions in [19, 17]). For strictly positive  $\sigma \in C^2(\Omega)$  satisfying  $\sigma \equiv 1$  near  $\partial\Omega$ , define  $q = \sigma^{-1/2}\Delta\sigma^{1/2}$  inside  $\Omega$ , continue  $q$  as zero outside  $\Omega$ , and set

$$\mathbf{t}(k) = \int_{\mathbb{R}^2} e^{ikz+i\bar{k}\bar{z}} q(z)m(z,k)dz, \quad (6.1)$$

where  $k \neq 0$  and  $m$  is the solution of  $m = 1 - g_k * (qm)$ . It can be shown that the substitution  $\mathbf{t}(0) = 0$  results in a continuous function  $\mathbf{t} : \mathbb{C} \rightarrow \mathbb{C}$ . We remark that the work of Knudsen [13] shows that formula (6.1) can be generalized for conductivities with only one weak derivative.

The scattering transform  $\tau$  of Astala and Päivärinta is given by the formula

$$\overline{\tau(k)} = \frac{1}{2\pi} \int_{\mathbb{C}} \bar{\partial}_z(\omega(z,k) - \omega^-(z,k)) dz_1 dz_2, \quad (6.2)$$

where  $\omega^-(z,k)$  corresponds to  $-\mu$  in the same way that  $\omega$  corresponds to  $\mu$ . For sufficiently smooth  $\sigma$ , the following formula gives a connection between the scattering transforms (6.1) and (6.2):

$$\mathbf{t}(k) = -4\pi i \bar{k} \tau(k). \quad (6.3)$$

However, the right hand side of (6.3) is defined for  $L^\infty$  conductivities as well.

The term *nonlinear Fourier transform* stems from the fact that linearizing  $\mathbf{t}$  with respect to  $q$  by substituting 1 in place of  $m$  in the right hand side of (6.1) gives the Fourier transform of  $q$ . Of course, this interpretation is not strictly valid for  $\mathbf{t}$  defined via (6.3) for nonsmooth  $\sigma$  since  $q$  is no more defined as a function. However, we continue to use the term in a generalized sense.

Now let  $\Lambda_\sigma$  and  $\Lambda_1$  be the Dirichlet to Neumann maps corresponding to  $\sigma$  and the constant conductivity 1, respectively. In medical electric impedance tomography one is dealing with a discontinuous (piecewise smooth) conductivity  $\sigma$ , and (6.1) is not defined. However, the formula

$$\mathbf{t}^{\text{exp}}(k) = \int_{\partial\Omega} e^{i\bar{k}\bar{z}} (\Lambda_\sigma - \Lambda_1) e^{ikz} dS(z) \quad (6.4)$$

is a kind of Born approximation, introduced in [20] and makes sense for  $L^\infty$  conductivities as well. Further, as shown in [16, 14],  $\mathbf{t}^{\text{exp}}(k)$  can be used to approximate  $\mathbf{t}(k)$  at least for  $k$  near zero and  $\sigma$  smooth. Using  $\mathbf{t}^{\text{exp}}$  in practical reconstructions from measured data is known to produce useful images [11, 12].

Thus, it is interesting to compare  $\mathbf{t}^{\text{exp}}(k)$  to the right hand side of (6.3) in case of discontinuous conductivities. Such a comparison has so far been possible only for differentiable conductivities.

### 6.1. Approximate computation of $\mathbf{t}$

We numerically evaluate the functions  $\tilde{\omega}_L(z, k)$  and  $\tilde{\omega}_L^-(z, k)$  and the approximation  $\tau_L$  to (6.2) defined by

$$\overline{\tau_L(k)} := \frac{1}{2\pi} \int_{\Omega} \bar{\partial}_z (\tilde{\omega}_L(z, k) - \tilde{\omega}_L^-(z, k)) dz_1 dz_2. \quad (6.5)$$

The results of Sections 2 and 3 can be used to show that the error in  $\tilde{\omega}_L(z, k)$  and  $\tilde{\omega}_L^-(z, k)$  becomes small when  $L$  is large.

**Theorem 4.** *Let  $\tau$  be defined by (6.2) and  $\tau_L$  by (6.5). Then for any  $k \in \mathbb{C}$*

$$\lim_{L \rightarrow \infty} \tau_L(k) = \tau(k).$$

**Proof.** Recall that

$$\begin{aligned} \bar{\partial}\omega &= (I - e_{-k}\mu\bar{S})^{-1}(\alpha\bar{\omega} + \alpha), \\ \bar{\partial}\omega^- &= -(I + e_{-k}\mu\bar{S})^{-1}(\alpha\bar{\omega} + \alpha). \end{aligned}$$

Expanding the Neumann series and using the fact that  $\mu$  is supported in  $\Omega$  shows that

$$\bar{\partial}\omega(z, k) = 0 \text{ and } \bar{\partial}\omega^-(z, k) = 0 \text{ when } |z| > 1.$$

It follows from (6.2) and Theorem 2 that

$$\overline{\tau(k)} = \frac{1}{2\pi} \int_{\Omega} \bar{\partial}_z (\tilde{\omega}(z, k) - \tilde{\omega}^-(z, k)) dz_1 dz_2. \quad (6.6)$$

Note that the domain of integration in (6.6) is  $\Omega$ , while in (6.2) it is  $\mathbb{R}^2$ .

Let  $\epsilon > 0$  be as in (2.8) and define an annulus  $\mathcal{A}_\epsilon$  as follows:

$$\mathcal{A}_\epsilon := \{z \in \mathbb{C} \mid 1 < |z| < 1 + \epsilon/2\}.$$

The constructions in the proof of Theorem 2 implies that

$$\bar{\partial}_z \tilde{\omega}(z, k) = 0 = \bar{\partial}_z \tilde{\omega}^-(z, k) \quad \text{for } z \in \mathcal{A}_\epsilon, \quad (6.7)$$

so we can write using Stokes' formula

$$\begin{aligned}\overline{\tau(k)} &= \frac{1}{2\pi} \int_{|z| < 1+\epsilon/4} \bar{\partial}_z(\tilde{\omega}(z, k) - \tilde{\omega}^-(z, k)) dz_1 dz_2 \\ &= \frac{1}{2\pi} \int_{|z|=1+\epsilon/4} (\tilde{\omega}(z, k) - \tilde{\omega}^-(z, k)) dS(z).\end{aligned}\quad (6.8)$$

The construction in the proof of Theorem 3 implies that

$$\bar{\partial}_z \tilde{\omega}_L(z, k) = 0 = \bar{\partial}_z \tilde{\omega}_L^-(z, k) \quad \text{for } z \in \mathcal{A}_\epsilon, \quad (6.9)$$

so applying Stokes' formula to (6.5) leads to

$$\overline{\tau_L(k)} = \frac{1}{2\pi} \int_{|z|=1+\epsilon/4} (\tilde{\omega}_L(z, k) - \tilde{\omega}_L^-(z, k)) dS(z). \quad (6.10)$$

Formulas (6.7) and (6.9) show that the functions  $\tilde{\omega}(\cdot, k)$ ,  $\tilde{\omega}^-(\cdot, k)$ ,  $\tilde{\omega}_L(\cdot, k)$  and  $\tilde{\omega}_L^-(\cdot, k)$  are analytic in  $\mathcal{A}_\epsilon$ , and Theorem 3 shows that

$$\begin{aligned}\lim_{L \rightarrow \infty} \|\tilde{\omega}(\cdot, k) - \tilde{\omega}_L(\cdot, k)\|_{L^2(\mathcal{A}_\epsilon)} &= 0, \\ \lim_{L \rightarrow \infty} \|\tilde{\omega}^-(\cdot, k) - \tilde{\omega}_L^-(\cdot, k)\|_{L^2(\mathcal{A}_\epsilon)} &= 0.\end{aligned}$$

Now  $L^2$  convergence and analyticity combined implies pointwise convergence, so the integral in (6.10) converges to the integral in (6.8) as  $L \rightarrow \infty$ .

Q.E.D.

### 6.2. Numerical results for rotationally symmetric cases

Let us define two simple conductivities with rotational symmetry and a jump discontinuity:

$$\sigma_1(z) = \begin{cases} 1.1 & \text{for } |z| < 1/2, \\ 1 & \text{otherwise,} \end{cases} \quad \sigma_2(z) = \begin{cases} 2 & \text{for } |z| < 1/2, \\ 1 & \text{otherwise.} \end{cases}$$

See the left column of Figure 5 for plots of profiles of  $\sigma_1$  and  $\sigma_2$ .

It is well-known that the Dirichlet-to-Neumann maps  $\Lambda_{\sigma_1}$  and  $\Lambda_{\sigma_2}$  can be expanded analytically in the trigonometric basis on the unit circle, see e.g. [20, Lemma 4.1]. Utilizing this we evaluate  $\mathbf{t}_1^{\text{exp}}(k)$  and  $\mathbf{t}_2^{\text{exp}}(k)$  very accurately with formula (6.4), see the solid line plots in the right column of Figure 5.

We evaluate  $\tilde{\omega}_L(z, k)$  and  $\tilde{\omega}_L^-(z, k)$  corresponding to both conductivities using the algorithm described in Section 4. Here  $k$  is real-valued and ranges in the interval  $[0.1, 19.6]$ . It is enough to compute using real  $k$  only since the symmetry  $\sigma(z) = \sigma(|z|)$  implies  $\mathbf{t}^{\text{exp}}(k) = \mathbf{t}^{\text{exp}}(|k|)$  and  $\mathbf{t}(k) = \mathbf{t}(|k|)$ .

Since the conductivities are nonsmooth, we cannot use the benchmark method for checking the accuracy of the computation by comparison as in Section 5.3. Instead we compute  $\tilde{\omega}_L(z, k)$  and  $\tilde{\omega}_L^-(z, k)$  on the two grids  $\mathcal{G}_8$

$\sigma_1(|z|)$  $\sigma_2(|z|)$  $|z|$  $|k|$ 

Figure 5: Left column: profiles of two rotationally symmetric example conductivities with a jump discontinuity. Right column: profiles of  $\mathbf{t}^{\text{exp}}$  (thick solid line) and  $\mathbf{t}$  (thin dotted line) evaluated using equation (6.3). Note that  $\mathbf{t}^{\text{exp}}$  and  $\mathbf{t}$  are not expected to coincide.

and  $\mathcal{G}_9$ , and compare the results on the points belonging to  $\mathcal{G}_8$ . The relative sup norm error between the two computations is less than 5% for  $k < 6.6$ , less than 10% for  $k < 12.6$ , and at most 21% in the whole  $k$  interval. Of course, we expect the result computed on  $\mathcal{G}_9$  to be more accurate, as is the case in the situation summarized in Table 1. Thus we have good reason to believe that the computation is reasonably accurate in the whole  $k$  interval.

We can now evaluate the scattering transforms  $\mathbf{t}_1$  and  $\mathbf{t}_2$  using (6.5) and (6.3). The functions  $\mathbf{t}_1$  and  $\mathbf{t}_2$  are plotted with thin dotted lines in the right column of Figure 5.

As mentioned above, there is inaccuracy in the computation of  $\tilde{\omega}_L(z, k)$  and  $\tilde{\omega}_L^-(z, k)$ . Also, numerical differentiation in the implementation of the right hand side of (6.5) may amplify the errors. Thus it is reasonable to doubt the accuracy of the plot of  $\mathbf{t}(k)$  in Figure 5, especially for large  $|k|$ . Let us make one more numerical test to estimate the size of error.

We define one more rotationally symmetric conductivity called  $\sigma_3$  as fol-

$\sigma_3(|z|)$

$|z|$

$|k|$

Figure 6: Left: profile of the rotationally symmetric example conductivity  $\sigma_3$ . Right: approximate profiles of  $\mathbf{t}$  computed using the benchmark method (thick solid line) and the new method (thin dotted line); note that these two functions are expected to coincide, but there is significant difference between them near  $k = 0$ . This is due to the inaccuracy of the benchmark method; the new algorithm performs clearly better for small  $k$  since  $\mathbf{t}$  is a continuous function and  $\mathbf{t}(0) = 0$ . For large  $|k|$  the computations agree remarkably well.

lows: define  $\zeta(t) := 1 - 10t^3 + 15t^4 - 6t^5$  and set

$$\sigma_3(z) = \begin{cases} 2 & \text{for } |z| < 3/10, \\ 1 & \text{for } |z| > 7/10, \\ 1 + \zeta\left(\frac{10(|z|-3/10)}{4}\right) & \text{otherwise.} \end{cases}$$

See the left plot of Figure 6 for the profile of  $\sigma_3$ . Now  $\sigma_3 \in C^4(\Omega)$  so that we can evaluate  $\mathbf{t}$  using the benchmark method and formula (6.1). The right plot of Figure 6 shows the results of these two methods of computation. For large  $|k|$  they agree very nicely, and for small  $|k|$  there is significant error. The inaccuracy near the origin comes from the benchmark algorithm since  $\mathbf{t}$  is known to be a continuous function and  $\mathbf{t}(0) = 0$ , so the new method is seen to be accurate for small  $|k|$  as well. The test thus suggests that the computations in Figure 5 are accurate.

### 6.3. Numerical results for a discontinuous heart-and-lungs phantom

We construct a simple discontinuous conductivity modelling a cross-section of human chest, see Figure 7. Note that this conductivity does not have any symmetries. We compute the corresponding functions  $\mathbf{t}^{\text{exp}}$  from (6.4) and  $\mathbf{t}$  using (6.5) and (6.3), see Figure 8.

### 6.4. Discussion of scattering transforms

The right column of Figure 5 illustrates how the linearized  $\mathbf{t}_1^{\text{exp}}$  approximation is quite close to the actual scattering transform  $\mathbf{t}_1$  in the case of the low

Figure 7: Simulated discontinuous conductivity (heart-and-lungs phantom).

Real( $\mathbf{t}^{\text{exp}}(k)$ )

Imag( $\mathbf{t}^{\text{exp}}(k)$ )

Real( $\mathbf{t}(k)$ )

Imag( $\mathbf{t}(k)$ )

Figure 8: Functions  $\mathbf{t}^{\text{exp}}(k)$  and  $\mathbf{t}(k)$  corresponding to a discontinuous conductivity (heart-and-lungs phantom of Figure 7). Here  $k$  ranges in the disc with center at origin and radius 4. Note that the two functions are not expected to coincide; rather  $\mathbf{t}^{\text{exp}}$  can be seen as an approximation to  $\mathbf{t}$ .

contrast conductivity  $\sigma_1$ . However, a larger difference is observed between the two functions in the case of the higher-contrast conductivity  $\sigma_2$ ; this is due to nonlinear effects. Also, in the case of the heart-and-lungs phantom inspired by the medical EIT application we see that  $\mathbf{t}^{\text{exp}}$  approximation is quite close to the actual scattering transform  $\mathbf{t}$ . This observation is consistent with the successful use of  $\mathbf{t}^{\text{exp}}$  in practical reconstructions from measured data [11, 12].

Another important evidence available in Figure 5 is the fact that  $|\mathbf{t}_1(k)|$  and  $|\mathbf{t}_2(k)|$  seem to take larger values as  $k$  grows. This is caused by the discontinuity in the conductivity: recall that for  $\sigma \in C^{2+m}(\Omega)$  and  $m \geq 1$  we know that  $|\mathbf{t}(k)| \leq |k|^{-m}$  for large  $|k|$ , see [20, Theorem 3.2]. This decay can be seen also in numerical computations of  $\mathbf{t}$  for smooth conductivities, see Figure 6 and [16, Section 5].

## 7. Numerical evidence for decay estimates

It was proven in [1] that  $f_\mu$  can be written in the form  $f_\mu(z, k) = e^{ik\phi_\mu(z, k)}$ , where  $\lim_{k \rightarrow \infty} \phi_\mu(z, k) = z$  uniformly in  $z \in \mathbb{C}$ . In this section we compute numerically the norms

$$\sup_{z \in \Omega} \left| \frac{1}{ik} \log(e^{-ikz} f_\mu(z, k)) \right| = \sup_{z \in \Omega} |\phi_\mu(z, k) - z| \quad (7.1)$$

corresponding to two rotationally symmetric conductivities, one smooth and another with a jump discontinuity. See the left plot in Figure 9 for profiles of the conductivities.

Our computation yields numerical evidence for the existence of an estimate of the form  $\sup_{z \in \Omega} |\phi_\mu(z, k) - z| \leq C|k|^\lambda$  with  $\lambda < 0$ , at least for simple smooth and piecewise smooth conductivities. See Figure 9. Curiously, it seems that the norm for smooth example does not decay significantly faster than the norm for the discontinuous example.

Let us report one further numerical test. While  $\sup_{z \in \Omega} |\phi_\mu(z, k) - z|$  evidently decays when  $k \rightarrow \infty$  as seen in Figure 9, the norms of the functions  $\omega(\cdot, k)$  do not. See Figure 10.

## 8. Speed, accuracy, and hardware issues

All computations were done with Matlab 7.5 using a computer called Akaatti (<http://alpha.cc.tut.fi/akaatti/>) located at Tampere University of Technology. The routines were not parallelized but run in a single node using a dual core 2.2 GHz AMD Opteron processor equipped with 4 gigabytes of random access memory.

Since Akaatti is in shared use and our computations may be delayed unexpectedly, we decided to measure computation times with a stand-alone

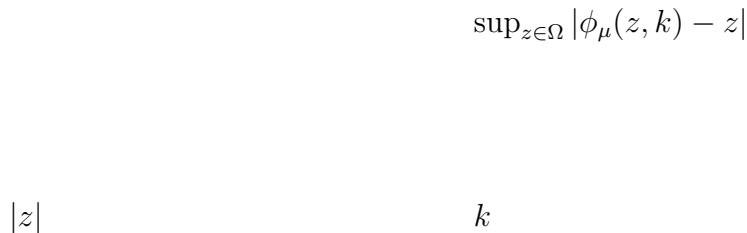


Figure 9: Left: profiles of two rotationally symmetric example conductivities. Right:  $\sup_{z \in \Omega} |\phi_\mu(z, k) - z|$  as defined in (7.1) corresponding to the conductivities to the left. The plot on the right suggests that in addition to the limit at  $k \rightarrow \infty$  being zero, a decay estimate could hold.

computer. The computer is a Lenovo T61p laptop with a dual core 2.4 GHz Intel Centrino Pro processor equipped with 3 gigabytes of random access memory. With the laptop, computation of  $\tilde{\omega}_L(\cdot, k)$  for a fixed  $k$  takes roughly one minute on the  $256 \times 256$  grid, and 7 minutes on the  $512 \times 512$  grid.

This is an initial feasibility study for a new CGO solver for Beltrami equation, and extensive work on reducing the computation time is outside the scope of this paper. However, let us point out few possibilities for optimizing the code:

- Instead of separating the real and imaginary parts and using the GMRES solver, it may be possible to construct a faster dedicated iterative solver for (3.4) analogously to the method developed by Eirola, Huhtanen, and von Pfaler in [7].
- Using a preconditioner in GMRES could speed up the computation considerably. However, designing a good preconditioner for the present context may not be straightforward.
- Our algorithm is naturally parallelizable since computation of  $\tilde{\omega}_L(z, k)$  can be done independently for each  $k$  value.
- Our approach could allow a two-grid extension similarly to the Lippmann-Schwinger case discussed in [24].

Full accuracy analysis for the new method would be valuable. This may require some refinements in the algorithm, such as more careful grid approximation for piecewise smooth functions as explained in [24].

$k$  $k$ 

Figure 10: Left: plot of the norms  $\|\tilde{\omega}_L(\cdot, k)\|_{L^2(\Omega)}$  as function of  $k$ ; here  $k$  is real-valued and ranges in  $0 \leq k \leq 20$ . Right: plot of the norms  $\|\tilde{\omega}_L(\cdot, k)\|_{L^\infty(\Omega)}$  as function of  $k$ . Dashed line in both plots corresponds to the smooth conductivity shown in the left plot in Figure 9, and solid line corresponds to the discontinuous conductivity.

## 9. Acknowledgments.

This material is based upon work supported by the National Science Foundation under Grant No. 0513509 (J. Mueller) and by the Finnish Centre of Excellence in Inverse Problems Research (Academy of Finland CoE-project 213476, L. Päivärinta and S. Siltanen) and by the Finnish Center of Excellence in Analysis and Dynamics Research (Academy of Finland projects 1118634 and 118422, K. Astala). During part of the preparation of this work, SS worked as professor at the Department of Mathematics of Tampere University of Technology.

## References

- [1] K. Astala and L. Päivärinta, *Calderón's inverse conductivity problem in the plane*, Ann. of Math., 163 (2006), pp. 265–299.
- [2] J. Bikowski and J. L. Mueller, *2D EIT reconstructions using Calderón's method*, Inverse Problems and Imaging, 2 (2007), pp. 43–61.
- [3] R. M. Brown and G. Uhlmann, *Uniqueness in the inverse conductivity problem for nonsmooth conductivities in two dimensions*, Comm. Partial Differential Equations, 22 (1997), pp. 1009–1027.
- [4] A. P. Calderón, *On an inverse boundary value problem*, In Seminar on Numerical Analysis and its Applications to Continuum Physics, Soc. Brasileira de Matemática (1980), pp.65–73.
- [5] M. Cheney, D. Isaacson and J. C. Newell, *Electrical Impedance Tomography*, SIAM Review, 41 (1999), pp. 85–101.

- [6] P. Daripa, *A fast algorithm to solve the Beltrami equation with applications to quasiconformal mappings*, Journal of Computational Physics, 106 (1993), pp. 355–365.
- [7] T. Eirola, M. Huhtanen, and J. Von Pfaler 2003 *Solution methods for  $\mathbb{R}$ -linear problems in  $\mathbb{C}^n$*  SIAM. J. Matrix Anal. & Appl. 25, pp. 804–828
- [8] L. D. Faddeev, *Increasing solutions of the Schrödinger equation*, Sov. Phys. Dokl., 10 (1966), pp. 1033–1035.
- [9] D. Gaydashev and D. Khmelev, *On numerical algorithms for the solution of a Beltrami equation*, arXiv:math.NA/0510516 (2005)
- [10] M. Ikehata and S. Siltanen, *Numerical solution of the Cauchy problem for the stationary Schrödinger equation using Faddeev’s Green function*, SIAM J. Appl. Math. 64 (2004), pp. 1907–1932.
- [11] Isaacson D, Mueller J L, Newell J and Siltanen S 2004, *Reconstructions of chest phantoms by the  $d$ -bar method for electrical impedance tomography*, IEEE Transactions on Medical Imaging 23 (2004), pp. 821–828.
- [12] Isaacson D, Mueller J L, Newell J and Siltanen S 2006, *Imaging Cardiac Activity by the  $D$ -bar Method for Electrical Impedance Tomography*, Physiological Measurement 27 (2006), pp. S43–S50.
- [13] K. Knudsen, *On the Inverse Conductivity Problem*, Ph.D. thesis, Department of Mathematical Sciences, Aalborg University, Denmark (2002).
- [14] Knudsen K, Lassas M, Mueller J L and Siltanen S,  *$D$ -bar method for electrical impedance tomography with discontinuous conductivities*, SIAM Journal of Applied Mathematics 67 (2007), pp. 893–913.
- [15] K. Knudsen, J. L. Mueller and S. Siltanen. *Numerical solution method for the  $d$ -bar-equation in the plane*. J. Comp. Phys. 198 (2004) pp. 500–517.
- [16] J. L. Mueller and S. Siltanen. *Direct reconstructions of conductivities from boundary measurements*. SIAM J. Sci. Comp., **24** (2003) pp.1232–1266.
- [17] Nachman A I 1988 Reconstructions from boundary measurements *Ann. of Math.* 128 531–576
- [18] A. I. Nachman, *Global uniqueness for a two dimensional inverse boundary value problem*, Ann. of Math. 143 (1996), pp. 71–96.

- [19] R.G. Novikov and G.M. Khenkin. The  $\bar{\partial}$ -equation in the multidimensional inverse scattering problem. *Uspekhi Mat. Nauk.*, 42:93–152, 1987.
- [20] S. Siltanen, J. Mueller and D. Isaacson *An implementation of the reconstruction algorithm of A. Nachman for the 2-D inverse conductivity problem*, Inverse Problems 16 (2000), pp.681-699
- [21] E. Stein *Singular integrals and differentiability properties of functions*, Princeton Mathematical Series, No. 30 Princeton University Press, Princeton, NJ, 1970.
- [22] J. Sylvester and G. Uhlmann. A global uniqueness theorem for an inverse boundary value problem. *Annals of Mathematics*, 125:153–169, 1987.
- [23] G. Vainikko, Multidimensional weakly singular integral equations, Lecture notes in mathematics 1549, Springer 1993.
- [24] G. Vainikko, Fast solvers of the Lippmann–Schwinger equation, in *Direct and Inverse Problems of Mathematical Physics* (Newark, DE), Kluwer Acad. Publ, Dordrecht, Int. Soc. Anal. Appl. Comput. **5**, 423 (2000).